Sensorless vector controlled synchronous reluctance motor fed by matrix converter

Sensorless Vector Controlled Synchronous Reluctance Motor Fed by Matrix Converter

Arzhang Yousefi-Talouki, and Gianmario Pellegrino
Department of Energy (DENERG)
Politecnico di Torino
Torino, Italy
arzhang.yousefitalouki@polito.it, gianmario.pellegrino@polito.it

***Abstract*—In this paper a sensorless control method is presented for a matrix converter-fed synchronous reluctance motor. The method includes low speed and standstill operating regions. The fields of applications are aerospace actuators where sensorless control augments the reliability of the drive, and robustness towards harsh ambient temperatures. The simulation results show the effectiveness of the presented method.**

Keywords—Flux Observer, Matrix Converter, Sensoreless Control, Synchronous Reluctance Motor

I. INTRODUCTION

Closed loop controlled synchronous reluctance motor (SyRM) drives recently reemerged to the industry as a reliable and efficient alternative to other ac drives [1-3]. The main feature and strength of this drive compared to the other ac counterparts are a competitive cost and high efficiency, due to the absence of rotor Joule losses.

One disadvantage of SyRM drives in industrial applications comes from to the need of the position sensor for closed loop control. For this reason, position sensorless techniques exist and are every day more adopted. Sensorless techniques were extensively studied for PM excited machines, and, to a lesser extent, for SyRM drives. When speed and frequency are high enough, back electromotive force (EMF) based methods can be adopted [4-5]. However, these methods fail to estimate the rotor position at low speeds and standstill. Thanks to the rotor saliency of synchronous machines, rotor position estimation is feasible at low and even zero speeds. To do so, high frequency signals are superimposed to the fundamental components to explore the rotor saliency and extract the position information [6-7]. In [8], Sul *et al.* first presented a method combing back-EMF and signal injection method for SyRM drives. However, the magnetic saturation of *d* and *q*-axis flux components is disregarded in this work, where constant L_d and L_q values were considered. Also, there is cross saturation between *d*-axis and *q*-axis flux components. Cross saturation produce an error in rotor position estimation, when using high frequency signal injection, as first demonstrated in [9]. In many cases, this aspect is disregarded in the literature of sensorless control, for cross saturation is not always evident in PM synchronous machines. On the contrary, it is evident in SyR machines. A *d* flux and *q* current vector control method based on flux observer was presented in [9-10]. In this method, the *d*-axis flux linkage and *q*-axis current are the control variables. The position is estimated at high speed through back-EMF integration, while at low speeds and standstill sensorless control is based on high frequency signal injection method. The high frequency signal is superimposed to the *d*-axis flux linkage. One of the advantages of this method is that the cross saturation effect is inherently compensated, provided that the flux observer has comprehensive knowledge of the machines parameters, in the form of *dq* flux linkage tables.

Matrix converters (MCs) have emerged as an attractive direct ac-ac alternative to conventional indirect ac-ac converter schemes [11-12]. MCs hold many advantages, including an adjustable input power factor, bidirectional power flow, high-quality power output waveforms and the lack of bulky capacitors. The diffusion of this kind of converters is expanding in some industries such as aerospace actuators and electrical motor drives [13-14]. Despite the advantages of matrix converter especially in the application where weight and volume are of importance, it seems that they can be promising in combination with SyR motors. However, to the authors' knowledge, the literature on this topic is very limited [15].

In this paper, a sensorless control method is proposed for a MC-fed SyR motor. The adopted sensorless method is the one presented in [10]. The modulation technique of MC is indirect space vector modulation [18]. In order to have an accurate flux estimation, the nonlinear voltage error of the MC is identified and compensated.

The concept presented in the paper opens the stage to a vaster application of SyRM drives in weight and volume critical applications.

II. SENSORLESS CONTROL METHOD

The SyR motor used in this paper is a 2.2 kW, 1500 rpm prototype [2]. The magnetic curves of the machine are shown in Fig.1. The dynamic model of SyRM in *dq* rotor frame is:

$$v_{dq} = Ri_{dq} + j\omega\lambda_{dq} + \frac{d\lambda_{dq}}{dt} \quad (1)$$

$$\begin{cases}\lambda_d = \lambda_d(i_d, i_q) \\ \lambda_q = \lambda_q(i_d, i_q)\end{cases} \tag{2}$$

$$T = \frac{3}{2}p\left(\lambda_d i_q - \lambda_q i_d\right) \tag{3}$$

The magnetic curves show evident cross saturation:

$$\frac{\partial \lambda_d}{\partial i_q} = \frac{\partial \lambda_q}{\partial i_d} = L_{dq} \neq 0 \tag{4}$$

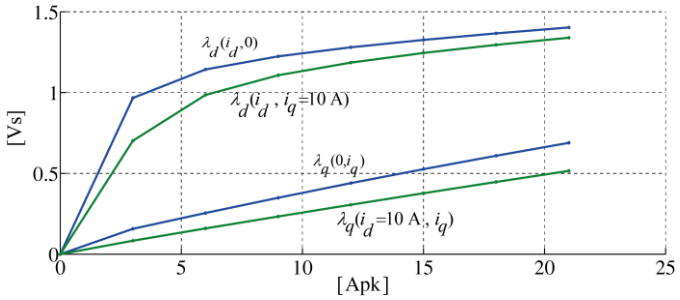

Fig. 1. Current to flux linkage curves of the machine under test

A. *Flux observer*

The flux observer used in this paper is illustrated in Fig.2. It has been proven in [1] that when an accurate magnetic model of motor is at hand, accurate flux observation at zero and low speed levels is possible. For high speed levels voltage integration is used for flux observation. The transfer function of this flux observer scheme is the one in (5). As can be seen, voltage integration ($v_{\alpha\beta} - Ri_{\alpha\beta}$) is high-pass filtered and flux linkage estimate from look-up table $\tilde{\lambda}_{\alpha\beta}$ is low-pass filtered according to the crossover angular frequency G [rad/s].

$$\hat{\lambda}_{\alpha\beta} = \frac{s}{s+G}\left(\frac{v_{\alpha\beta} - Ri_{\alpha\beta}}{s}\right) + \frac{G}{s+G}\tilde{\lambda}_{\alpha\beta} \tag{5}$$

G is also the error gain of the observer, and sets the crossover speed between high and low speed models. As a consequence, this observer has a good performance in a wide speed range.

B. *Sensorless rotor angle and speed observer*

In most of the literature dedicated to SyRMs, these are closed loop current controlled. However, it has been proved in [1] that if the control variables are (λ_d, i_q), instead, the drive response becomes independent from the grade of core saturation. Moreover, such scheme is also more robust at high speed towards core loss and rotor angle error effects. As shown in Fig.2, *d*-axis flux linkage is obtained from flux observer ($\hat{\lambda}_d$). In addition, it is evident that the knowledge of rotor angle is compulsory for flux observation.

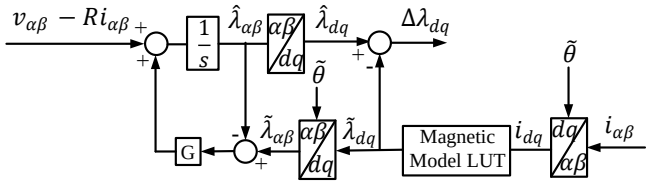

Fig. 2. Block diagram of the flux observer

In the high-speed region ($\omega > G$), the observed flux linkage ($\hat{\lambda}_{\alpha\beta}$) tracks the current model estimated flux linkage ($\tilde{\lambda}_{\alpha\beta}$). Thus, rotor position ($\tilde{\theta}$) can be estimated by use of inverse coordinate transformation, as in (6), and used for coordinate transformation in Fig. 2.

$$\sin(\tilde{\theta}) = \frac{\hat{\lambda}d\tilde{\lambda}_\beta - \hat{\lambda}q\tilde{\lambda}_\alpha}{\lambda^2} \qquad \cos(\tilde{\theta}) = \frac{\hat{\lambda}d\tilde{\lambda}_\alpha + \hat{\lambda}q\tilde{\lambda}_\beta}{\lambda^2} \tag{6}$$

Estimated speed follows (7), where T_s is the sampling period. For details, see [10].

$$T_s\tilde{\omega}_k = \sin\tilde{\theta}_k \cos\tilde{\theta}_{k-1} - \cos\tilde{\theta}_k \sin\tilde{\theta}_{k-1} \tag{7}$$

However, at zero and low speeds, voltage integration is prone to error and the scheme of Fig. 2 alone is not stable. Therefore, the observer is augmented with the injection of an 800 Hz *d* flux linkage component, superimposed to the *d* flux linkage reference to explore the machine saliency ($\lambda^*_{d,hf}$ in Fig. 3). The high-frequency signal is injected along the estimated *d* axis direction: if this coincides with the actual *d* axis of the rotor, then the high frequency component of flux in *q*-axis will be zero ($\tilde{\lambda}_{q,hf} = 0$). It has been shown in [9] that the flux observer error on q axis $\Delta\lambda_{q,hf} = \hat{\lambda}_{q,hf} - \tilde{\lambda}_{q,hf}$ can be usefully adopted as error signal to track the zero position error in place of $\tilde{\lambda}_{q,hf}$. Therefore, the position error signal $\Delta\lambda_{q,hf}$ is band-pass filtered and demodulated to isolate the presence of non-zero 800 Hz component, used as the input of the position tracking loop of Fig. 4. The tracking loop scheme shown in the figure uses the former position and speed estimates (6-7) as feedforward signals, for the sake of smooth transition between the signal injection-based and back-emf integration based position estimates: $\hat{\theta}$ and $\tilde{\theta}$, respectively. This tracking loop scheme guarantees a smooth transition between $\hat{\theta}$ and $\tilde{\theta}$ when the 800 Hz injection is turned off, and vice versa. Also, the estimated angle $\tilde{\theta}$ will track the observed one $\hat{\theta}$ also at zero and low speed, and hence rotor speed (7) will be correct over the entire speed range of the drive.

C. *Transition between low and high speed*

The crossover speed between high speed and low speed model is defined by G which is set to 35 [rad/s] equal to 167 rpm. Also, when rotor speeds reaches 477 rpm, the amplitude of injected flux starts to be reduced and at the speed of 596 rpm, the flux injection turns off, and vice versa.

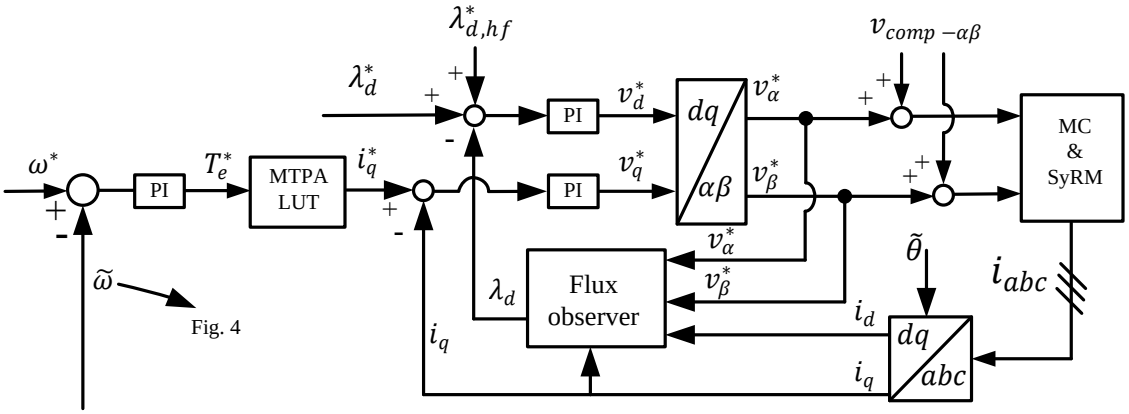

Fig. 3. Block diagram of the proposed control technique. The speen and position observer is presented in Fig.4

D. General control scheme

The block diagram of the drive control technique adopted in this paper is depicted in Fig.3. As previously mentioned, the flux linkage on *d*-axis and current on *q*-axis are the two control variables. High frequency flux injection ($\lambda^*_{d,hf}$) is evidenced in the figure.

Also, the reference value of i^*_q is determined by the torque reference through a maximum torque per ampere (MTPA) look-up table (LUT). Estimated speed used for closed loop control ($\tilde{\omega}$) comes from equation (7).

III. MATRIX CONVERTER APPLICATION TO SENSORLESS CONTROL

The Matrix Converter (MC) schematic diagram is shown in Fig.5. In this paper, double-sided switching pattern [17] is adopted for indirect space vector modulation strategy [18]. Also, four-step current based commutation method is used. As the adopted sensorless method is based on a flux observer, nonlinearities in matrix converter affect the accurate flux observation. The MC output voltage is affected by two main sources of error, coming from voltage drops of semiconductors in conduction and from edge uncertainty of current commutations. Hence, in this section, such nonlinear actuation errors of MCs are investigated and compensated.

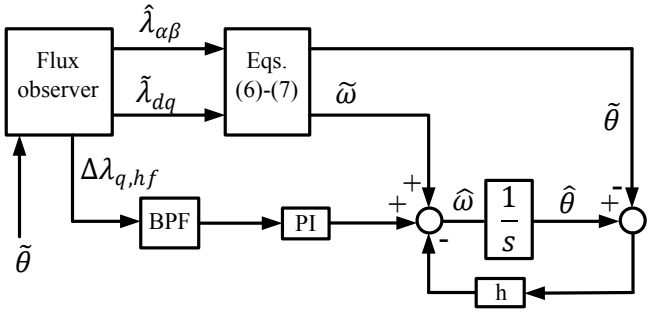

Fig. 4. Sensorless rotor speed and position angle observer.

A. Voltage drop effect

In this paper, voltage drops of IGBTs and free-wheeling diodes are considered in simplified manner [16]. The voltage drop across the devices is as (8). Coefficient "2" is due to this fact that in matrix converters two devices are always conducting. $V_{th}$is a fixed threshold value which is forward voltage of a power device.

$$V_{Di} = 2V_{th}sign\ (I_i) + R_d I_i\ ,\ i = \{a, b, c\} \qquad (8)$$

B. Voltage error due to current commutation

In matrix converters, when commutation is done to transfer the current from one output phase to another phase, an edge uncertainty voltage error is produced which is shown by V_{EU} [19]. As an example, if the input voltage of the converter is in sector 1, the produced V_{EU} is as (9) where V_A is input voltage phase-A, Tpwm is switching time, t_c is commutation time, and t_r and t_f are IGBT rising and falling time, respectively. The path of input phase voltage is depicted in Fig.6. As can be seen from (9) and Fig.6, V_A in sector 1 varies from a minimum value ($\frac{\sqrt{3}}{2}V_{pk}$) to a maximum value (V_{pk}). Hence the edge uncertainty voltage errors varies in a band. This concept is illustrated in Fig.7. By changing the sectors, V_A is replaced with two other input voltages (V_B and V_C) in (9).

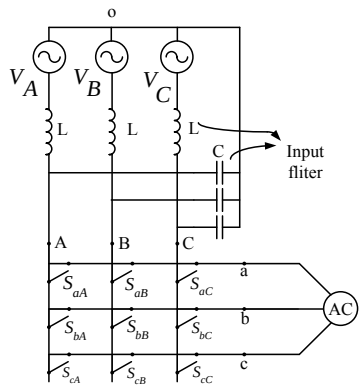

Fig.5: Schematic diagram of a three-phase matrix converter

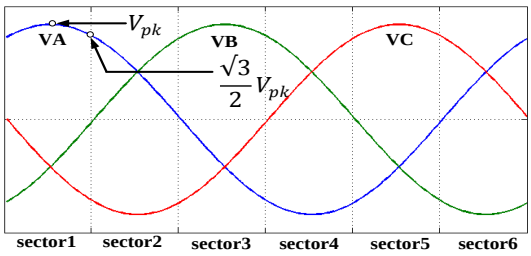

Fig.6: Input phase voltages and corresponding sectors

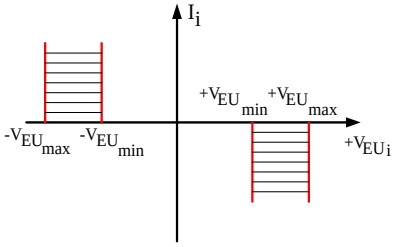

Fig.7: voltage edge uncertainty effect

$$V_{EU_i} = 3V_A \frac{t_c + t_f - t_r}{T_{pwm}}\, sign(I_i);\ i = \{a, b, c\} \qquad (9)$$

C. *Feedforward Compensation based on Signum Function*

A feedforward compensation scheme, based on signum function is used, illustrated in Fig.8. Signum function based voltage errors are evaluated for the three output phases and then transformed into two-phase components αβ. The compensation signals are indicated in Fig.3 as $V_{comp-\alpha\beta}$ and generated as in Fig. 8.

IV. SIMULATION RESULTS

The synchronous reluctance motor and matrix converter data is tabulated in Table I. Tests for different speed and load levels are presented. High frequency flux (800 Hz) is injected on *d*-axis. The amplitude of injected flux is 0.02 [Vs]. Also, rated λ_d^* is considered to be 0.9 [Vs]

TABLE I
Matrix converter and SyR specification

SyR motor	
Rated power/Number of poles	2.2 kW / 4
Nominal Speed/Rated Torque	1500 rpm / 14 Nm
Stator resistance	4.34 Ω
Matrix Converter	
EUPEC FM35R12KE3ENG module	
Switching device	1200 V, 35 A, IGBT
t_c	0.2 μs
t_f / t_r	65-90 ns / 30-45 ns
power	7.5 kW
AC input voltage	3×415 V

In the first test, the machine is closed loop controlled at zero speed. A step load (2 Nm) is applied to the motor at $t = 5\ s$. Speed waveform and current on *q*-axis are shown in Fig. 9 (a) and (b), respectively. Also, the error between actual and observed position is shown using $\sin(\hat{\theta} - \theta)$, where θ is the actual rotor position and $\hat{\theta}$is the observed one. This variable is shown in Fig.9 (c). As it can be seen, the error is very close to zero. Also, it has been discussed in section III that in order to have an accurate flux linkage observation, nonlinearities of MC were compensated. Figures 10 (a), (b), and (c) show the speed waveform, current on *q*-axis, and position error, respectively when compensation technique is not applied. As can be seen, when the compensation is OFF, the control is out of bound and position error is very high. Because at zero speed, voltage errors of MC are very evident.

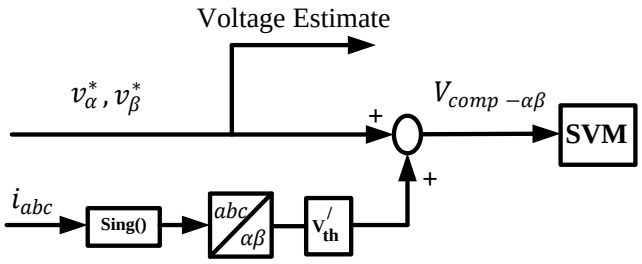

Fig.8: Feedforward compensation of MC voltage error

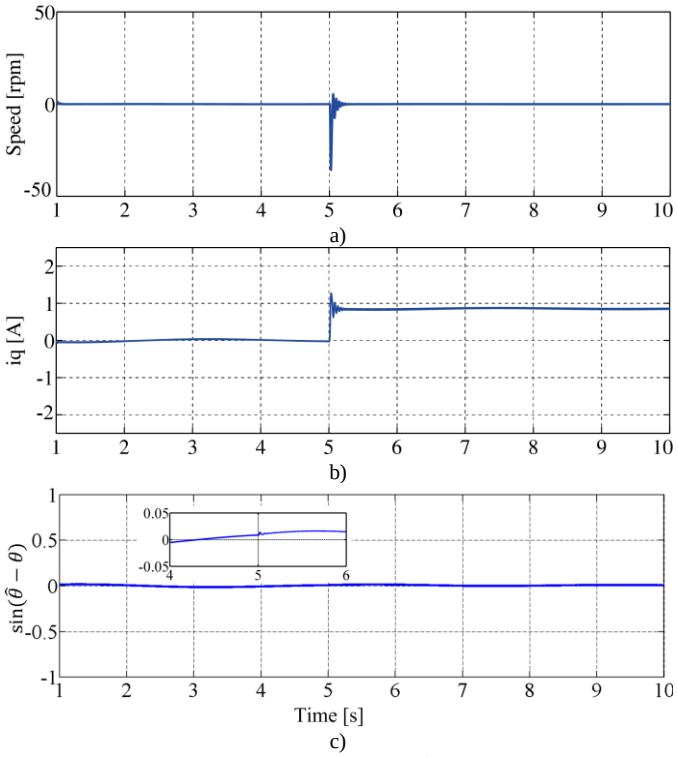

Fig. 9. Test at zero speed when compensation of MC errors is ON: a) speed waveform; b) current on *q*-axis; c) position error

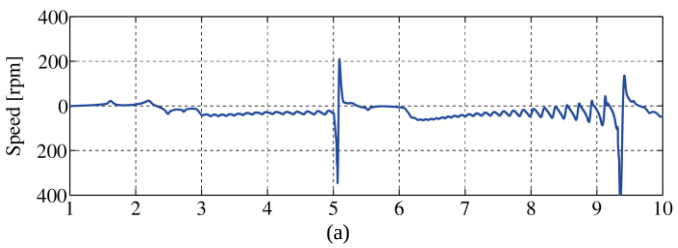

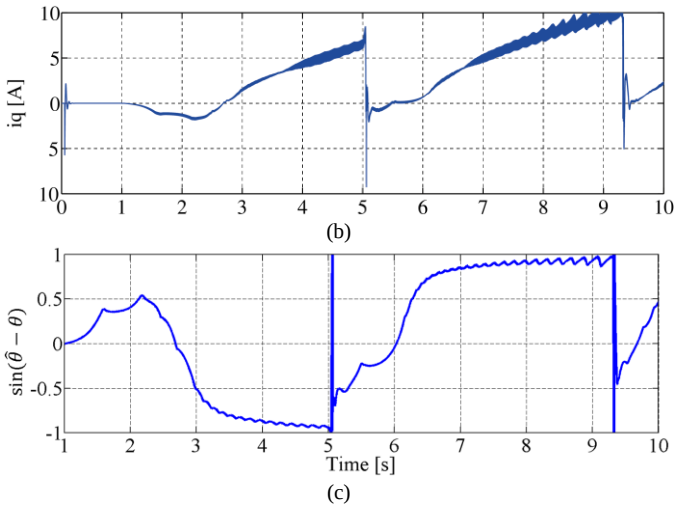

Fig. 10. Test at zero speed when compensation of MC errors is OFF: a) speed waveform; b) current on q-axis; c) position error

In the next test, motor is closed-loop speed controlled at 100 rpm. Motor accelerates at $t = 2\ s$ and again an step load is applied at $t = 5\ s$. Speed waveform, current on q-axis, and position error are shown in Fig.11 (a), (b), and (c), respectively. As it is seen, the speed is controlled at 100 rpm and the error between actual and observed rotor position is around zero. Also, these variables when compensation of MC nonlinear error is OFF is shown in figures 12 (a), (b), and (c), respectively. As can be seen, when motor accelerates, position error starts to be less dependent to the MC nonlinear errors.

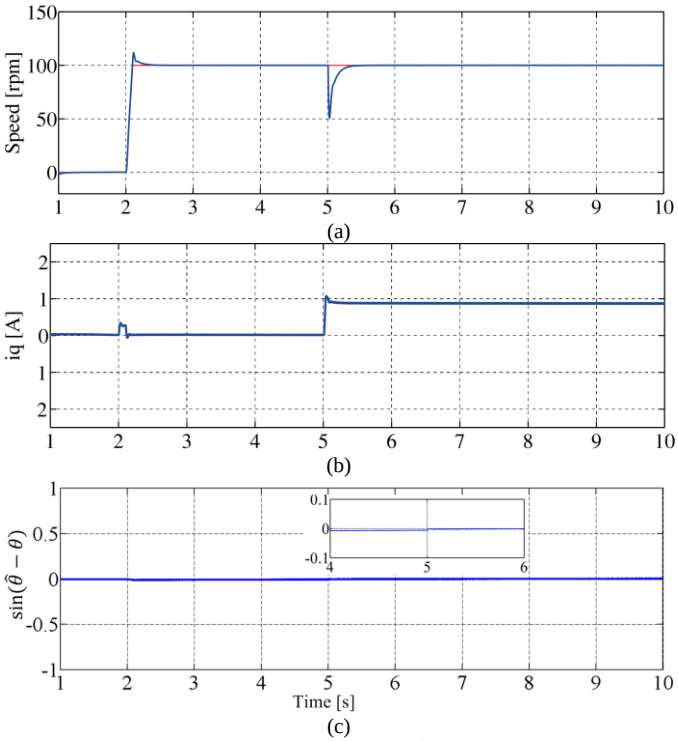

Fig. 11. Test at 100 rpm when compensation of MC errors is ON: a) speed wave form; b) current on q-axis; c) position error

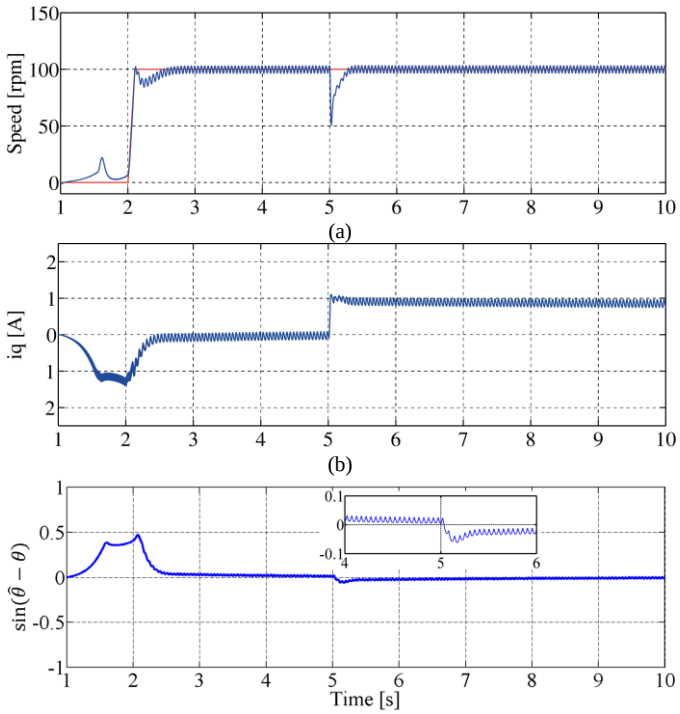

Fig. 12. Test at 100 rpm when compensation of MC errors is OFF: a) speed wave form; b) current on q-axis; c) position error

Finally, the response of the proposed drive is investigated in the transition back and forth from low speed to high-speed. In this test, motor accelerates at $t = 2\ s$ to reach 1500 rpm. At $t = 5\ s$ motor decelerates to the 100 rpm. Also, a positive step load torque is applied at time 4 s and then reversed at time 7 s. As explained in section II, at high speeds there is no high frequency injection which can be seen in Fig.13 (b). It is evident that when the motor accelerates to the high speeds, flux injection stops and starts again when motor decelerates. Speed, current on q-axis, and position error are shown in figures 13 (c), (d), and (e), respectively. Speed variation produces transient position error, but limited within acceptable bounds (< 0.03 rad = 1.7 °).

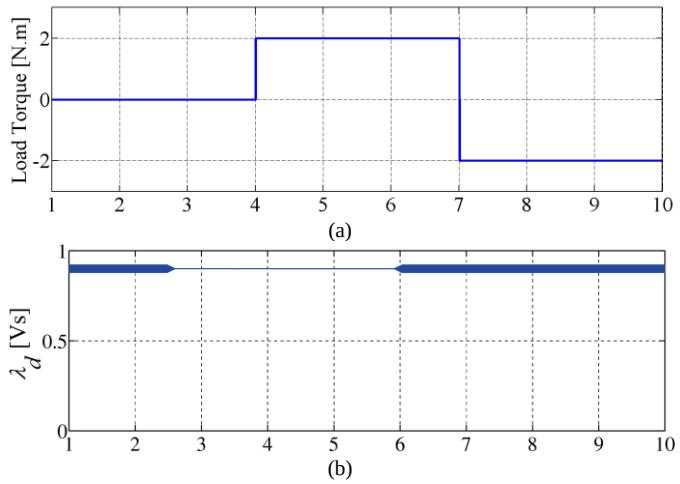

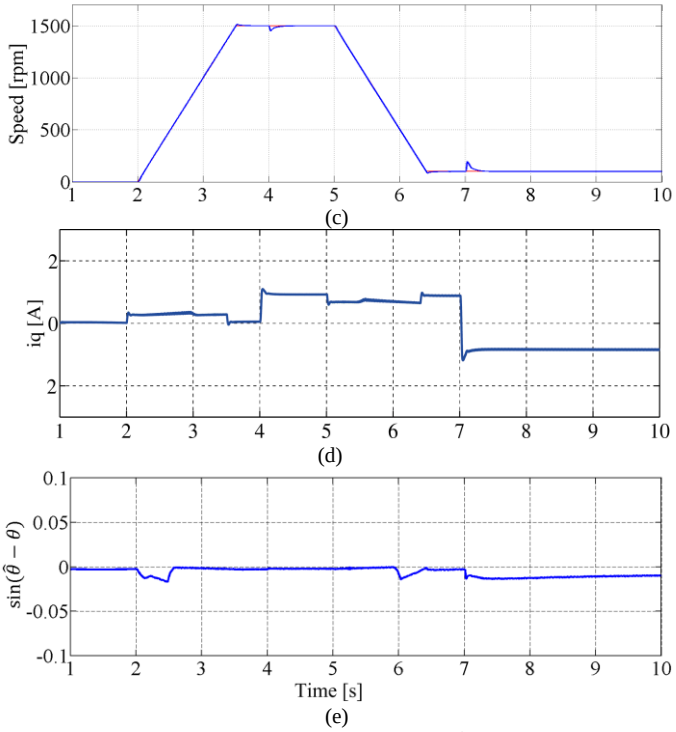

Fig. 13. Test at 100 rpm and 1500: a) load torque; b) flux linkage on *d*-axis; c) speed waveform; d) current on q-axis; e) position error

V. CONCLUSION

This paper proposes the sensorless control of a MC supplied SyRM drive, meant for high efficiency and high compactness applications. A high frequency flux injected to the *d*-axis flux linkage in order to estimate the rotor position at low speed levels. At high speeds, the sensorless control is based on back-EMF integration. The hybrid flux and current vector controller takes advantage of the flux observer information, and requires the knowledge of the machine magnetic parameters and the compensation of the converter voltage error. Nonlinear voltage errors of matrix converter are identified and compensated. Future work will be devoted to experimental validation of the proposed concept.

REFERENCES

[1] Vagati, A.; Pastorelli, M.; Franceschini, G., "High-performance control of synchronous reluctance motors,"Industry Applications, IEEE Transactions on, vol.33, no.4, pp.983,991, Jul/Aug 1997.

[2] Boglietti, A.; Cavagnino, A.; Pastorelli, M.; Vagati, A., "Experimental comparison of induction and synchronous reluctance motors performance," Industry Applications Conference, 2005. Fourtieth IAS Annual Meeting. Conference Record of the 2005 , vol.1, no., pp.474,479 Vol. 1, 2-6 Oct. 2005.

[3] Hofmann, H.F.; Sanders, S.R.; El-Antably, A., "Stator-flux-oriented vector control of synchronous reluctance Machines with maximized efficiency," Industrial Electronics, IEEE Transactions on , vol.51, no.5, pp.1066,1072, Oct. 2004.

[4] Piippo, A.; Hinkkanen, M.; Luomi, J., "Analysis of an Adaptive Observer for Sensorless Control of Interior Permanent Magnet Synchronous Motors," Industrial Electronics, IEEE Transactions on , vol.55, no.2, pp.570,576, Feb. 2008.

[5] Lagerquist, R.; Boldea, I.; Miller, T.J.E., "Sensorless-control of the synchronous reluctance motor," Industry Applications, IEEE Transactions on , vol.30, no.3, pp.673,682, May/Jun 1994.

[6] Agarlita, S.-C.; Boldea, I.; Blaabjerg, F., "High-Frequency-Injection-Assisted "Active-Flux"-Based Sensorless Vector Control of Reluctance Synchronous Motors, With Experiments From Zero Speed," Industry Applications, IEEE Transactions on , vol.48, no.6, pp.1931,1939, Nov.-Dec. 2012.

[7] e Kock, H.W.; Kamper, M.J.; Kennel, R.M., "Anisotropy Comparison of Reluctance and PM Synchronous Machines for Position Sensorless Control Using HF Carrier Injection," Power Electronics, IEEE Transactions on , vol.24, no.8, pp.1905,1913, Aug. 2009.

[8] Seog-Joo Kang; Jang-Mok Kim; Seung-Ki Sul, "Position sensorless control of synchronous reluctance motor using high frequency current injection," Energy Conversion, IEEE Transactions on , vol.14, no.4, pp.1271,1275, Dec 1999.

[9] Guglielmi, P.; Pastorelli, M.; Vagati, A., "Impact of cross-saturation in sensorless control of transverse-laminated synchronous reluctance motors," Industrial Electronics, IEEE Transactions on , vol.53, no.2, pp.429,439, April 2006.

[10] Capecchi, E.; Guglielmi, P.; Pastorelli, M.; Vagati, A., "Position-sensorless control of the transverse-laminated synchronous reluctance motor," Industry Applications, IEEE Transactions on, vol.37, no.6, pp.1768,1776, Nov.-Dec. 2001

[11] Wheeler, P.W.; Rodriguez, J.; Clare, J.C.; Empringham, L.; Weinstein, A., "Matrix converters: a technology review," Industrial Electronics, IEEE Transactions on , vol.49, no.2, pp.276,288, Apr 2002.

[12] Rodriguez, J.; Rivera, M.; Kolar, J.W.; Wheeler, P.W., "A Review of Control and Modulation Methods for Matrix Converters," Industrial Electronics, IEEE Transactions on , vol.59, no.1, pp.58,70, Jan. 2012.

[13] Xiaoyan Huang; Goodman, A.; Gerada, C.; Youtong Fang; Qinfen Lu, "A Single Sided Matrix Converter Drive for a Brushless DC Motor in Aerospace Applications," Industrial Electronics, IEEE Transactions on , vol.59, no.9, pp.3542,3552, Sept. 2012.

[14] Dan Xiao; Rahman, M.F., "Sensorless Direct Torque and Flux Controlled IPM Synchronous Machine Fed by Matrix Converter Over a Wide Speed Range," Industrial Informatics, IEEE Transactions on , vol.9, no.4, pp.1855,1867, Nov. 2013.

[15] Yousefi-Talouki, A.; Pellegrino, G., " Vector contro of matrix converter-fed synchronous reluctance motor based on flux observer, "Electrical Machines Design Control and Diagnosis (WEMDCD), 2015 IEEE Workshop on, 26-27 March 2015.

[16] Kyo-Beum Lee; Blaabjerg, F., "A nonlinearity compensation method for a matrix converter drive," Power Electronics Letters, IEEE , vol.3, no.1, pp.19,23, March 2005.

[17] Casadei, D.; Serra, G.; Tani, A.; Zarri, L., "Matrix converter modulation strategies: a new general approach based on space-vector representation of the switch state," Industrial Electronics, IEEE Transactions on , vol.49, no.2, pp.370,381, Apr 2002.

[18] Huber, L.; Borojevic, D., "Space vector modulated three-phase to three-phase matrix converter with input power factor correction," Industry Applications, IEEE Transactions on , vol.31, no.6, pp.1234,1246, Nov/Dec 1995.

[19] Arias, A.; Empringham, L.; Asher, G.M.; Wheeler, P.W.; Bland, M.; Apap, M.; Sumner, M.; Clare, J.C., "Elimination of Waveform Distortions in Matrix Converters Using a New Dual Compensation Method," Industrial Electronics, IEEE Transactions on , vol.54, no.4, pp.2079,2087, Aug. 2007.